

# Constitutive Relations for AA 5754 Based on Crystal Plasticity

L. HU, A.D. ROLLETT, M. IADICOLA, T. FOECKE, and S. BANOVIC

Constitutive equations for the multiaxial stress-strain behavior of aluminum alloy 5754 sheets were developed, based on crystal plasticity. A Taylor-based polycrystal plasticity model, a tangent formulation of the self-consistent viscoplastic model (VPSC), and an N-site viscoplastic model based on the fast Fourier transform (VPFFT) were used to fit a single slip system hardening law to the available data for tension, plane strain, and biaxial stretching. The fitting procedure yields good agreement with the monotonic stress-strain data, with similar parameter values for each model. When simulating multiaxial tests using the developed hardening law, models that allow both stress and strain variations in grains give better predictions of the stress-strain curves. Furthermore, generally, the simulated texture evolution is too rapid when compared to the experiments. By incorporating a more detailed neighbor interaction effect, the VPFFT model predicts texture evolution in better agreement with experiments.

DOI: 10.1007/s11661-011-0927-1

© The Minerals, Metals & Materials Society and ASM International 2011

## I. INTRODUCTION

THE 5000-series magnesium-strengthened aluminum alloys are used for interior sheet components in automotive bodies. They have excellent weldability and corrosion resistance, providing a higher strength-to-weight alternative to steel that can enhance fuel economy, safety, and driving performance.<sup>[1]</sup> Simulations of forming processes are needed to manufacture parts efficiently from sheet aluminum metal. Such processes often involve complex loading paths. Therefore, accurate predictions of stress-strain relations and texture development, especially for multiaxial deformation and different strain paths, are required for reliable simulations of metal forming processes. In addition, knowledge of how the texture evolves with multiaxial plastic strain, and having a robust mathematical description of this behavior, is also useful as an input to thermomechanical processing of the sheet as a control of initial texture to improve formability.

Polycrystal plasticity models assume that strain hardening occurs through dislocation accumulation on each slip system with varying degrees of complexity of interactions among the systems in each grain. Thus, the basic constitutive law adopted for this work is that which describes the hardening behavior of an individual slip system.

Taylor-type models assume identical strains across the polycrystal.<sup>[2]</sup> Asaro and Needleman<sup>[3]</sup> developed a rate-dependent constitutive model based on the isostrain Taylor assumption that could account for arbitrary

large strain and individual grain rotation. With a code similar to the Taylor model code used in this work,<sup>[4]</sup> Kocks *et al.*<sup>[5]</sup> showed that polycrystal plasticity could be used to account for the differences in hardening between different strain modes in copper. Bronkhorst *et al.*<sup>[6]</sup> made predictions of pole figures and stress-strain curves, which they compared to copper experimental data from compression, tension, simple shear, and plane strain compression (only the stress and strain in the longitudinal direction considered) tests. It was shown that the Taylor model yielded good first-order agreement with the experiment.

Uniform strain assumption satisfies compatibility conditions but not the stress equilibrium across grain boundaries. Self-consistent (SC) approaches were developed to address the grain interaction in an average sense. Molinari *et al.*<sup>[7]</sup> presented a SC formulation for texture predictions in large deformation of viscoplastic polycrystals incorporating deformation heterogeneities. Lebensohn and Tomé<sup>[8]</sup> extended the formulation to a viscoplastic self-consistent (VPSC) model for the plastic deformation in viscoplastic polycrystals, in which a grain is treated as an inhomogeneity embedded in a HEM that has the average property of the polycrystal. Their model has been widely used for modeling material anisotropic behaviors. Choi *et al.*<sup>[9]</sup> investigated the macroscopic anisotropy in AA5019 sheets with both Taylor and VPSC models, and the VPSC model showed a better agreement with experimental data in yield stresses and  $R$  values.

The advance of the computational power enables full-field calculations of polycrystal constitutive behaviors. Moulinec and Suquet<sup>[10]</sup> proposed a method based on the fast Fourier transform (FFT) algorithm to compute the local and overall responses of nonlinear composites. Lebensohn<sup>[11]</sup> later adapted the FFT approach for viscoplastic polycrystals. Sampling data in a regular Fourier grid, the VPFFT model allows the response of every individual site to vary independently. Delannay *et al.*<sup>[12]</sup> made quantitative comparisons of texture

---

L. HU, Graduate Student, and A.D. ROLLETT, Professor, are with the Department of Materials Science and Engineering, Carnegie Mellon University, Pittsburgh, PA 15213. Contact e-mail: linhu@andrew.cmu.edu M. IADICOLA, Mechanical Engineer, T. FOECKE, Group Leader, and S. BANOVIC, Materials Research Engineer, are with the NIST Center for Metal Forming, National Institute of Standards and Technology, Gaithersburg, MD 20899-8553.

Manuscript submitted July 15, 2010.

Article published online November 2, 2011

predictions from several plasticity models and concluded that N-site models give improved predictions over Taylor-type models.

Whereas texture evolution is predominantly determined by the crystallographic nature of the available slip systems, no “first principles” model exists for strain hardening. Therefore, constitutive equations must be developed by fitting to experimental data. Throughout the years, constitutive relations based on crystal plasticity were well established for uniaxial loading, and comparisons between forming limit data and multiaxial numerical predictions were made. However, there is little discussion in the literature on predicting both stress-strain curves and texture development for processes that involve different loading paths for in-plane and multiaxial deformation. Moreover, texture development often only has been analyzed in a qualitative fashion.

In this study, the plastic response in AA5754 was simulated with a full-constraint (FC) Taylor model,<sup>[4]</sup> the tangent VPSC model,<sup>[8]</sup> and the N-site VPFFT model,<sup>[11]</sup> and compared to multiaxial stress-strain curves and texture evolutions from the experiment. The objective of the study is to establish constitutive equations that properly account for strain hardening and grain (*i.e.*, lattice) rotation during deformation. By incorporating such crystal plasticity based equations into plasticity models, the accuracy of predictions for stress-strain curves and texture evolutions can be improved.

## II. EXPERIMENT

The material used in this investigation was industrially processed AA5754-O sheet, nominally 1-mm thick. Its chemical composition is reported in Table I. The alloy derives most of its strength from the solid solution strengthening with magnesium atoms, interacting with dislocations, and inhibiting dynamic recovery processes during straining.<sup>[13]</sup>

The five strain paths investigated were equibiaxial tension, uniaxial tension in the rolling direction (RD), uniaxial tension transverse to the loading direction (TD), plane strain with the first principal strain in the RD (with near zero strain in the TD), and plane strain with the first principal strain in the TD (with near zero strain in the RD). The samples were tested in the plane of the sheet. Uniaxial testing was performed using dog-bone sheet tension specimens. Biaxial tension tests were performed using a technique based upon the Raghavan modification of the Marciniak biaxial stretching test.<sup>[14]</sup> This technique holds the sheet sample in a binder while the center area is stretched using a cylindrical ram with an edge radius (to form a cup shape in the sample).

Nearly linear strain ratios from equibiaxial to uniaxial (up to forming limit strains) can be achieved by reducing the specimen width and thus the amount of constraint in the reduced width direction. The presence of unquantifiable friction forces means that no simple relation between ram force and applied stress exists. Therefore, stresses are measured near the surface of the sheet directly above the centerline of the ram by a modified X-ray diffraction (XRD) residual stress measuring system.<sup>[14]</sup> The strains were measured simultaneously using a calibrated biaxial extensometer in contact with the surface of the sheet located slightly off-center so as to not interfere with the XRD stress measurement. Uniaxial samples were tested with, and without, XRD stress measurement, while using a calibrated uniaxial extensometer and calibrated load cell to verify the XRD measurements. The stress-strain data used in this article was measured using the XRD technique exclusively in order to produce a SC set.<sup>[15]</sup> Multiple tests were performed for the plane strain and biaxial tests to verify repeatability.

The textures of the samples were measured using XRD technique.<sup>[16]</sup> Three incomplete pole figures were measured with the tilt angle  $\alpha$  ranging from 0 to 65 deg, namely, {111}, {200}, and {220}. The full pole figures and three-dimensional (3-D) orientation distribution (OD, which gives the normalized probability density of finding a given texture component specified by the three Euler angles,  $\varphi_1$ ,  $\Phi$ , and  $\varphi_2$ ) were derived from the measured pole figures using the preferred orientation package from Los Alamos (popLA).<sup>[17]</sup>

## III. MODELING

Three polycrystal plasticity models were used to simulate the AA5754 response under the five different strain paths, namely, a FC Taylor model, a tangent VPSC model, and the N-site VPFFT model. The purpose of using the three different models was to explore the sensitivity of the constitutive fitting and texture development to the choice of model.

### A. Single-Crystal Constitutive Behavior

All three models assume the same rate-sensitive single-crystal constitutive behavior, Eq. [1].

$$\dot{\varepsilon}^0 = \gamma_0 \sum_{\alpha=1}^N m^{\alpha} \left| \frac{m^{\alpha} : \dot{\sigma}}{\dot{\tau}^{\alpha}} \right|^K \text{sgn}[m^{\alpha} : \dot{\sigma}] \quad [1]$$

Here,  $\dot{\varepsilon}^0$  and  $\dot{\sigma}$  are the plastic strain rate and stress,  $\gamma_0$  is the reference shear rate,  $N$  is the number of slip

Table I. Chemical Composition of AA5754 Used in the Study

Element	Mg	Mn	Fe	Si	Cr, Cu, Pb, Ni, Sn, Ti, Zn	Aluminum
Weight percent	3.75	0.29	0.24	0.06	individually <0.05	balance

systems,  $\hat{\tau}^\alpha$  is the critical resolved shear stress (CRSS) of the slip system, and  $\kappa$  is the power-law exponent (inverse of rate sensitivity).  $m^\alpha$  is the Schmid tensor for the slip system  $\alpha$  defined as

$$m^\alpha = \frac{1}{2}(b^\alpha \otimes n^\alpha + n^\alpha \otimes b^\alpha) \quad [2]$$

where  $b$  and  $n$  are the slip direction and slip plane normal.

Equation [1] is an implicit equation that is solved to find the stress state in each grain (or, at each Fourier point in the VPFFT model) that generates the prescribed strain rate. This is done in all the models. The skew-symmetric part of the slips is then used to update the grain orientation, which allows the Taylor factor to evolve with strain. As described in the next section, the magnitude of the slip on each system is used to evolve the CRSS during deformation in a grain. The physical basis for the stress increase is mainly attributed to the increase in dislocation density that occurs as dislocations on intersecting systems entangle with each other. Since dislocations interact with various barriers to their motion, such as other dislocations, grain boundaries, and dislocation cell walls, the constitutive relation that is fit to the data implicitly accounts for all contributions to flow stress. In this work, we only consider the case of

isotropic hardening; *i.e.*, each slip system hardens at the same rate. If strain path changes are considered, then more complex models may be required such as latent hardening.

## B. Strain Hardening

The Voce type strain hardening is adopted in the three models in slightly different forms. For the FC Taylor model, a strain-hardening rate  $\theta$  describes the evolution of CRSS  $\tau$  from an initial CRSS,  $\tau_0$ , toward a saturation value  $\tau_v$ :

$$\theta = \frac{d\tau}{d\Gamma} = \theta_0 \left(1 - \frac{\tau}{\tau_v}\right) \quad [3]$$

where  $\theta_0$  is the initial hardening rate and  $\Gamma$  is the shear on a given slip system. For the VPSC and  $n$ -site VPFFT models, an extended Voce hardening rule governs the isotropic strain hardening behavior:

$$\tau = \tau_0 + \tau_1 \left(1 - \exp\left(-\Gamma \frac{\theta_0}{\tau_1}\right)\right) \quad [4]$$

where  $(\tau_0 + \tau_1)$  is the back-extrapolated CRSS.

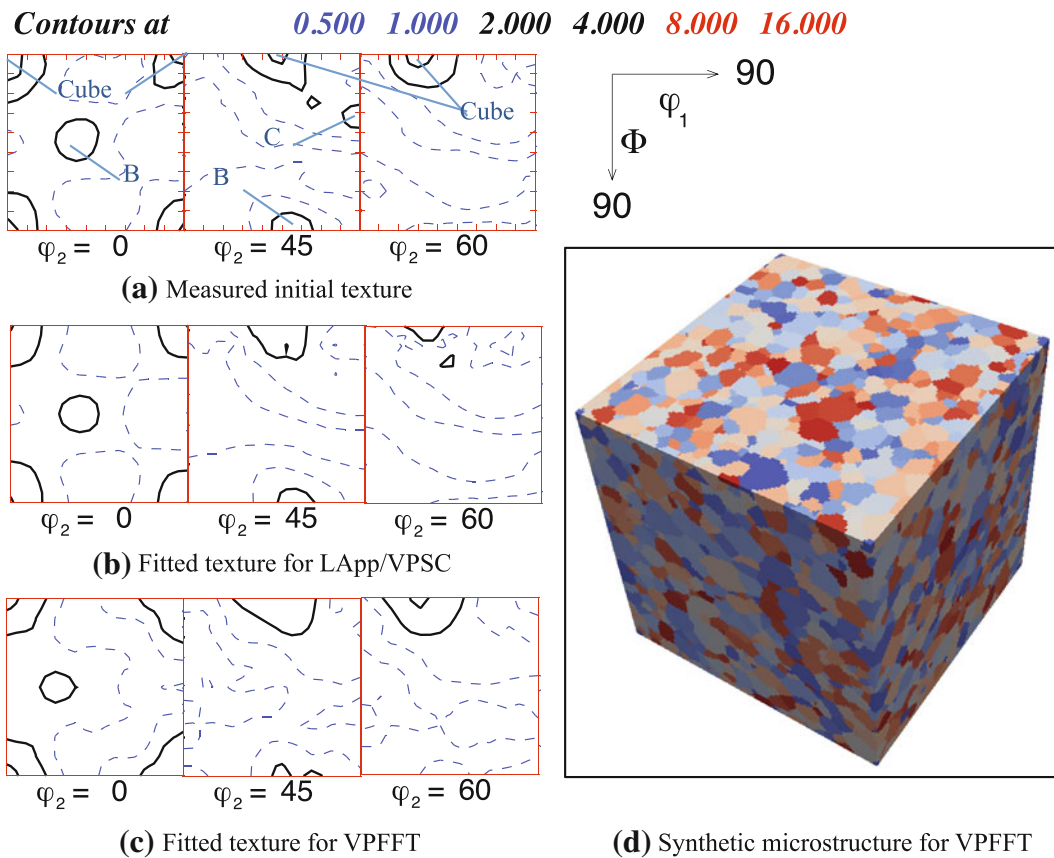


Fig. 1—Comparison of 0, 45, and 60 deg  $\varphi_2$  sections in (a) the experimental OD and fitted ODs for the (b) LApp, VPSC, and (c) VPFFT models. Locations of ideal texture components (Cube, Brass, and Copper) are noted. The unit for contour levels is multiples of random intensity. (d) The  $128 \times 128 \times 128$  synthetic microstructure for the VPFFT model with 5403 grains is shown. Colors denote different grains.

**Table II. Comparison of Cube, Brass, and Copper Volume Fractions; Euler Angles (Degrees) for Each Component Are Listed**

	Cube (0,0,0)	Brass (35,45,0)	Copper (90,35,45)
Uniform texture	0.0067	0.012	0.013
Experiment	0.024	0.027	0.022
LApp/VPSC	0.021	0.027	0.022
VPFFT	0.021	0.022	0.018

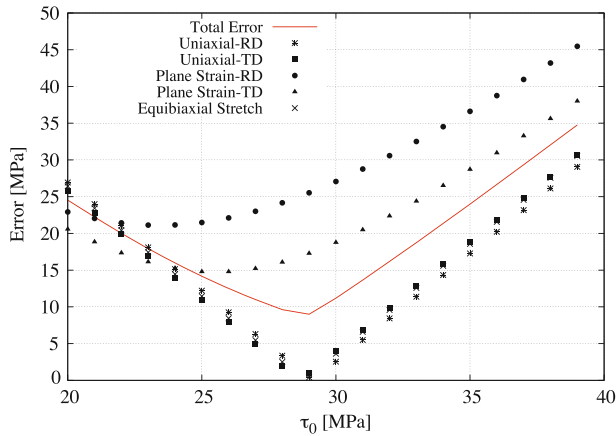


Fig. 2—Error vs the initial CRSS  $\tau_0$ . A single minimum of the total error is found at  $\tau_0 = 29$  MPa.

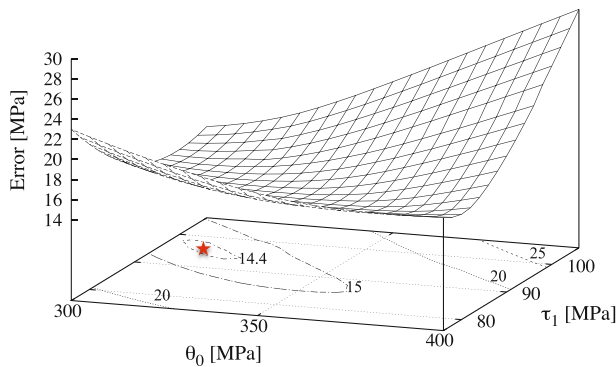


Fig. 3—3-D plot of the error vs the initial hardening rate  $\theta_0$  and CRSS  $\tau_1$ . The error values are projected on the bottom and plotted with contour levels. A single minimum is found at  $\{\theta_0, \tau_1\} = \{310, 96\}$ , noted by the star.

**Table III. Strain Hardening Parameters Fitted for the Plasticity Models**

	$\tau_0$ (MPa)	$\tau_1$ (MPa)	$\tau_v$ (MPa)	$\theta_0$ (MPa)
LApp	29	—	82	210
VPSC	33	96	—	310
VPFFT	32	80	—	320

### C. Grain Interaction

Assumptions on how grains interact link the effective response of polycrystalline aggregates to individual grain response. The three models have varying degrees of complexity for interactions between grains, from none in the Taylor-type models to all sites varying independently in the VPFFT model.

The FC Taylor model assumes a uniform strain on all grains. The applied macroscopic boundary condition is imposed on all grains, and averaging the grain behaviors gives the material response. The Taylor or Bishop–Hill solution in the rate-insensitive limit provides an upper bound approximate answer, which is then used as the initial estimate of the (deviatoric) stress in Eq. [1].

The tangent VPSC model allows each grain to interact with its surroundings in an average sense. The grain is treated as an ellipsoidal inclusion embedded in a homogeneous effective medium (HEM), the properties of which are not known *a priori* and are adjusted self-consistently to coincide with the average of all grains. Under the HEM assumption, the strain and stress in each grain varies as a function of orientation and the stiffness of the interaction, depending on the choice of homogenization methods for approximating a linear

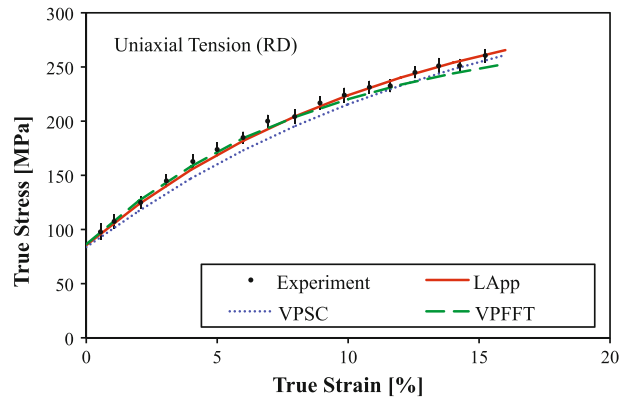


Fig. 4—Comparison of measured and simulated stress-strain curves for RD uniaxial tension.

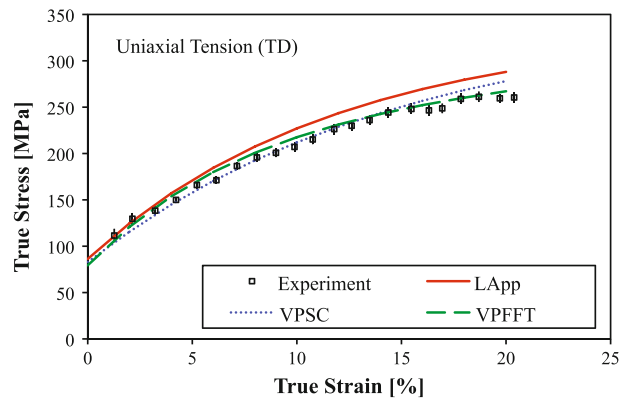


Fig. 5—Comparison of measured and simulated stress-strain curves for TD uniaxial tension.

behavior at grain level. The tangent approximation used in this study is obtained by a first-order Taylor expansion of the constitutive equation in the vicinity of overall response. It was shown that, opposed to the completely stiff body assumed in the Taylor model, the tangent scheme described a relatively compliant matrix in terms of the grain to matrix interaction.<sup>[18]</sup>

Whereas the VPSC model assumes homogeneous deformation inside the grains, the N-site VPFPT model takes into account the interaction of each point with all the other points in the (periodic) simulation volume. It provides a full-field solution to both the equilibrium and compatibility equations.

#### IV. SIMULATIONS

To simulate the stress-strain response and texture evolutions in AA5754, three plasticity codes were used, including the Los Alamos polycrystal plasticity (LApp) code based on the FC Taylor model,<sup>[4]</sup> the VPSC code

developed by Lebensohn and Tomé,<sup>[8]</sup> and the 3-D N-site VPFPT code developed by Lebensohn.<sup>[11]</sup> A weighted list of orientations was fitted to the measured initial texture as the input for the simulations. The material parameters used in the LApp and VPSC simulations were identified by the best fit (calculated with a cost function that sums the root-mean-square (RMS) differences between points) to the experimental values based on the stress-strain curves in the five mechanical tests being equally weighted in the error calculation. A simple

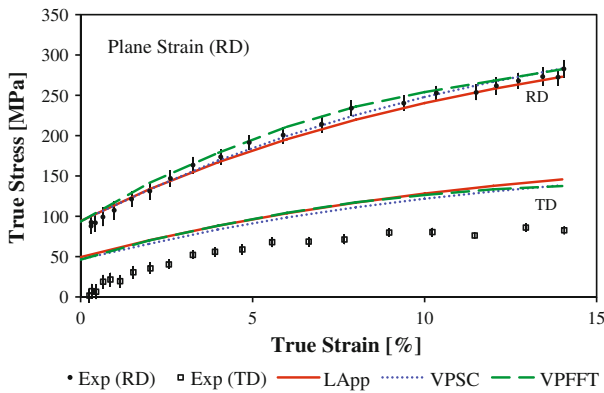


Fig. 6—Comparison of measured and simulated stress-strain curves for RD-oriented plane strain tension. The horizontal axis is the true strain in RD, and stresses both in RD and TD are plotted in the graph.

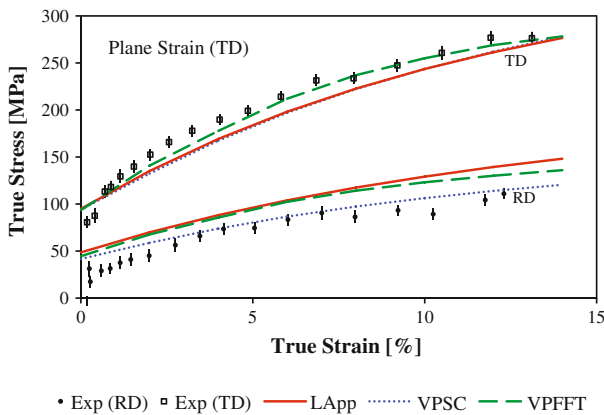


Fig. 7—Comparison of measured and simulated stress-strain curves for TD-oriented plane strain tension. The horizontal axis is the true strain in TD, and stresses both in RD and TD are plotted in the graph.

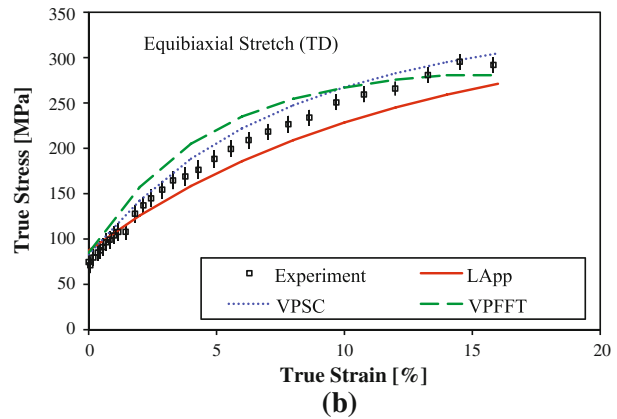
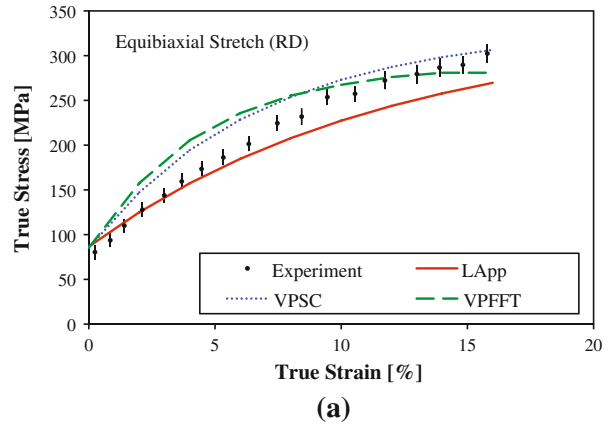


Fig. 8—Comparison of measured and simulated (a) RD and (b) TD stress-strain curves for equibiaxial stretch.

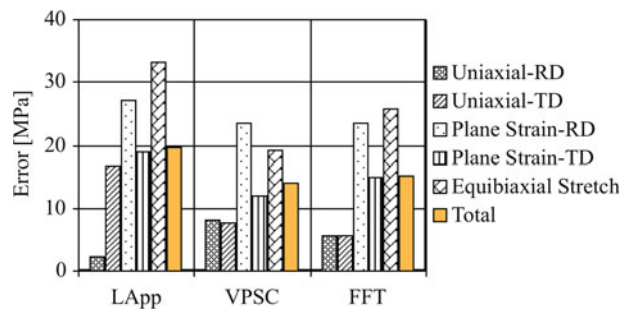


Fig. 9—Bar chart for the quality of fit to the experimental data in the five strain paths for the three different viscoplasticity models. The error value in the vertical axis is the RMS difference between the simulated stress-strain curves and the experimental data.

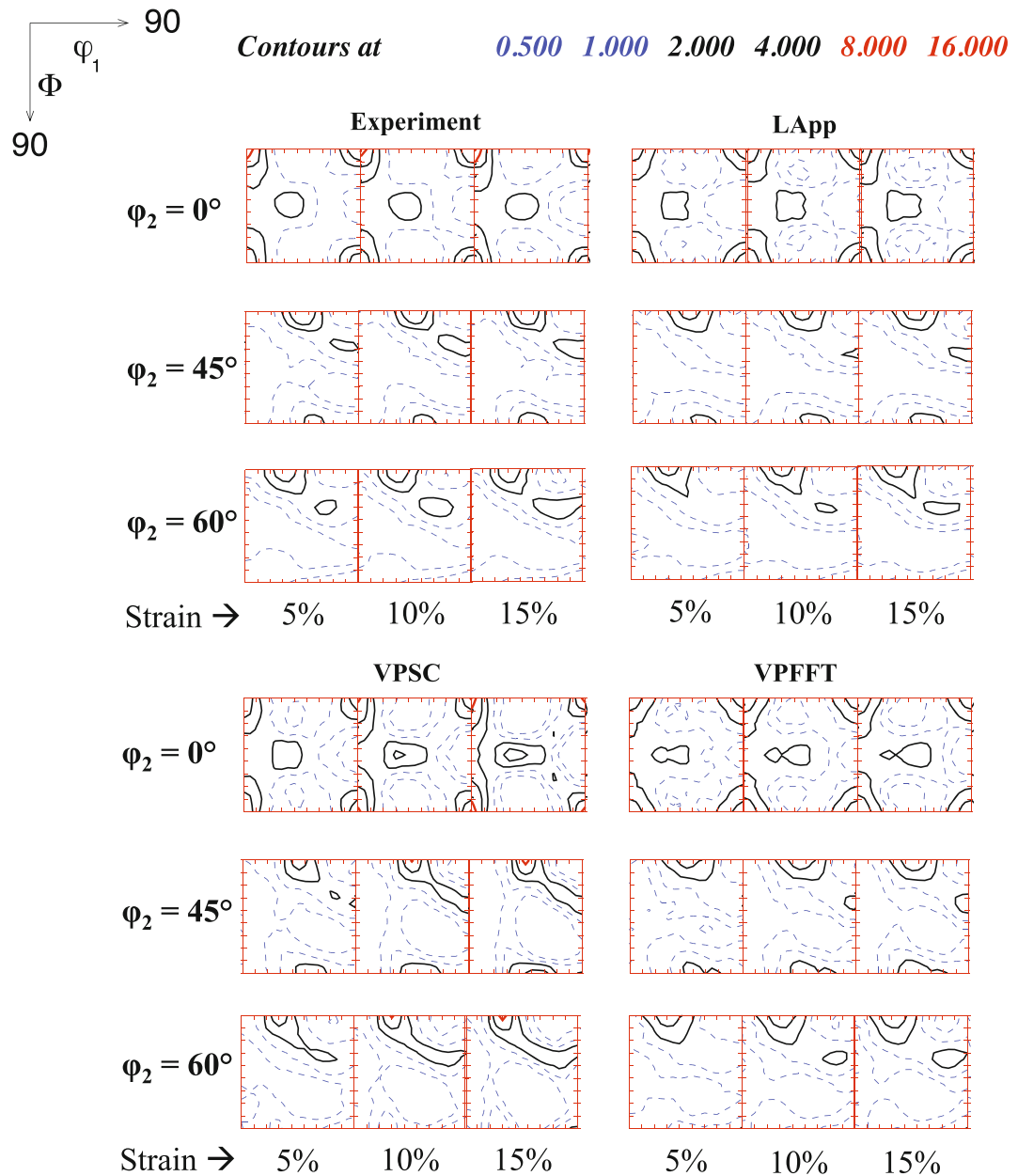


Fig. 10—Comparison of OD sections for RD uniaxial tension. Strain levels are 5, 10, and 15 pct in RD.

test grid of parameter values was used because of the small number of parameters to be fitted, which has the advantage of confirming that a global minimum exists in the cost function. The VPFFT simulation is significantly more time-consuming than LApp or VPSC, so the set of hardening parameters was manually selected, starting with the values determined for VPSC.

#### A. Fitting the Initial Texture

The fitting of the measured initial texture is required since the polycrystal is represented by weighted orientations in the plasticity modeling. Figure 1(a) presents the OD sections derived from the experimental pole figures of as-received AA5754-O sheet with ideal texture

components noted on the graphs. The sheet metal samples are weakly textured with a combination of recrystallization (Cube) and retained deformation (Brass and Copper) components.

The experimental OD was used to generate a weighted set of 24,938 discrete orientations that are representative of the texture. The discrete texture was used as the starting texture in the LApp and VPSC simulations. The weighted orientations after the plasticity simulation were rebinned into the OD space applying both cubic crystal symmetry and orthorhombic sample symmetry. The fitted texture is shown in Figure 1(b). In the VPFFT model, the polycrystalline microstructure takes the form of a representative volume element (RVE) with periodic boundary conditions and the RVE is discretized into a

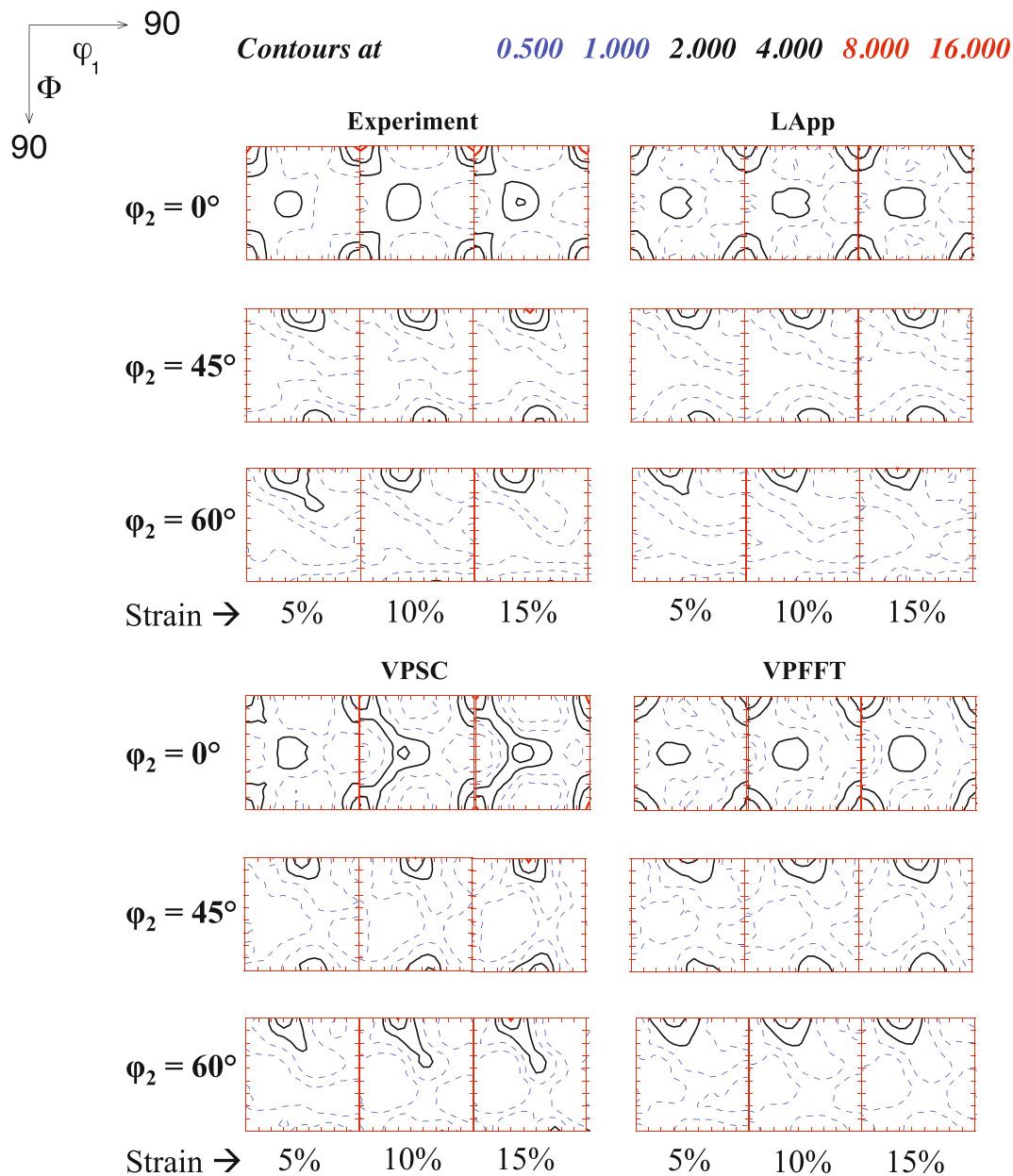


Fig. 11—Comparison of OD sections for TD uniaxial tension. The strain levels are 5, 10, and 15 pct in TD.

regular grid of points. A synthesized  $128 \times 128 \times 128$  microstructure of 5403 equiaxed grains, as shown in Figure 1(d), was built using the Microstructure Builder.<sup>[19]</sup> Fewer grains (than for the LApp and VPSC models) were used to avoid excessively long computing times. The equiaxed grain structure corresponds to the grain shapes observed experimentally.<sup>[16]</sup> Orientations of grains were assigned using an optimization technique to resemble the initial texture. The fitted texture for the VPFFT model is presented in Figure 1(c).

A good match between the measured and fitted textures can be seen from the comparison. To quantify the fitting, volume fractions of major components were calculated assuming a 10 deg orientation spread, as listed in Table II. A 5 deg discretization of the OD space

was used. Volume fractions for a random (uniform) texture are also included as a reference. The fitted texture well captured major texture components, especially for Cube, the intensity of which was almost 4 times random. The fitting was better for the LApp and VPSC models than the VPFFT model because of the smaller number of grains used in the latter model.

### B. Strain Hardening Parameter Fitting

The strain hardening parameters to be identified are the initial CRSS,  $\tau_0$ , the initial hardening rate,  $\theta_0$ , and the saturation CRSS,  $\tau_s$ , in the FC Taylor model (or  $\tau_1$  in the VPSC and VPFFT models), as in the hardening Eqs. [3] and [4]. Since the experimental data include

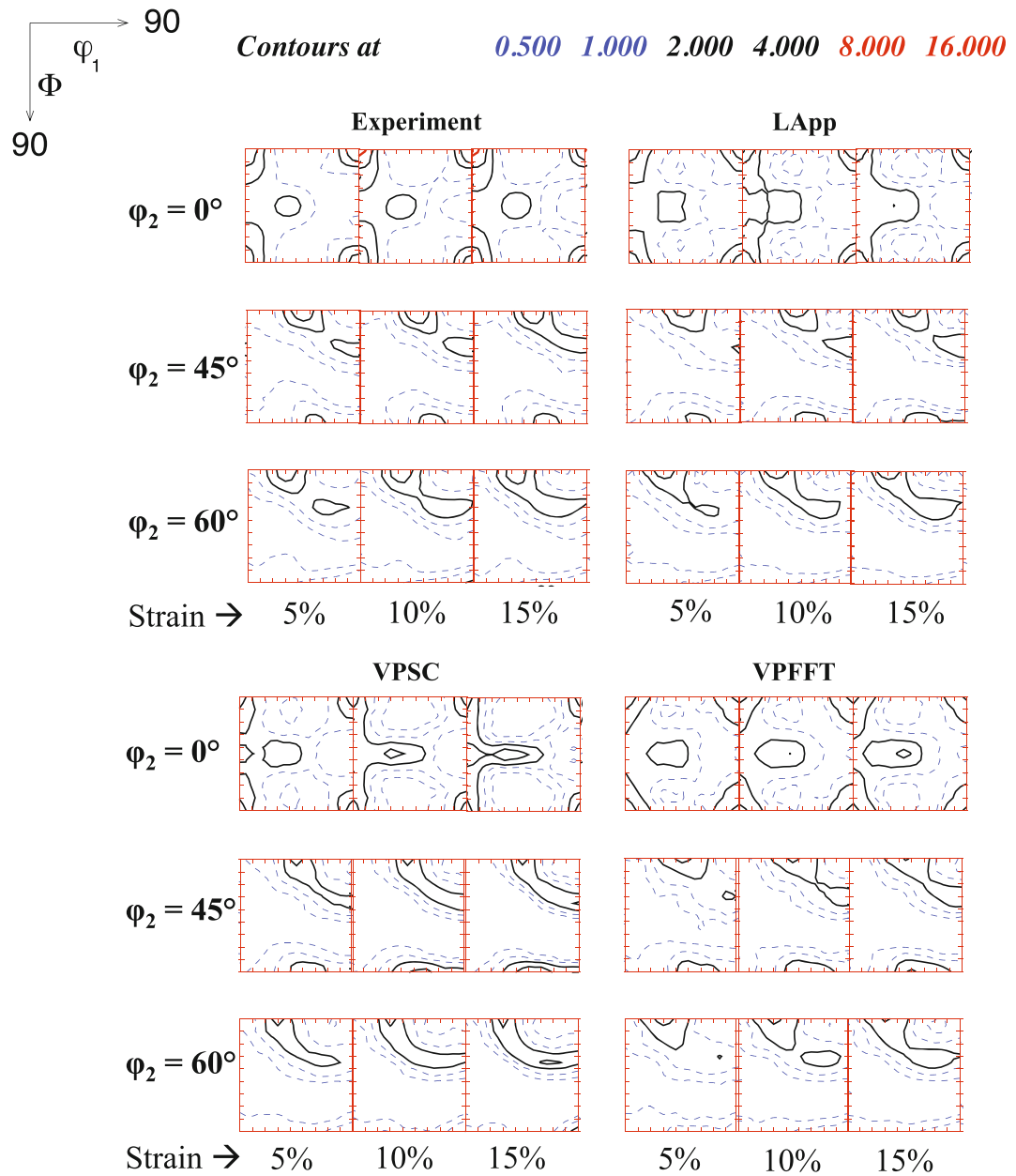


Fig. 12—Comparison of OD sections for RD-oriented plane strain tension. The strain levels are 5, 10, and 15, in RD.

five different strain paths (the RD uniaxial tension, the TD uniaxial tension, the RD plane strain, the TD plane strain, and the equibiaxial stretch), the objective was to determine a single set of hardening parameters to match the five stress-strain curves. The underlying assumption is that it is valid to use a single constitutive law at the single slip system level. To find the best match of the model predictions with the experimental data, we searched a range of hardening parameter values, sampling the parameter space on a regular grid to ensure that a unique minimum of the error value was identified. Although more expensive than, for example, a steepest descent method, the small number of parameters means that the complete set of simulations only requires a few hours on a standard desktop

and ensures that the minimum in the sampled parameter value range exists.

The error of a simulated stress-strain curve is calculated by the RMS difference from the experimental data:

$$\text{error} = \sqrt{\frac{\sum_{i=0}^n (S_i^{\text{simul}} - S_i^{\text{exp}})^2}{n + 1}} \quad [5]$$

where  $n$  is the strain steps at which the measurement was taken,  $S^{\text{simul}}$  is the stress value from the model, and  $S^{\text{exp}}$  is the measured stress value at the corresponding strain level. The total error for a given set of parameter values is the average of the error of the five stress-strain curves.

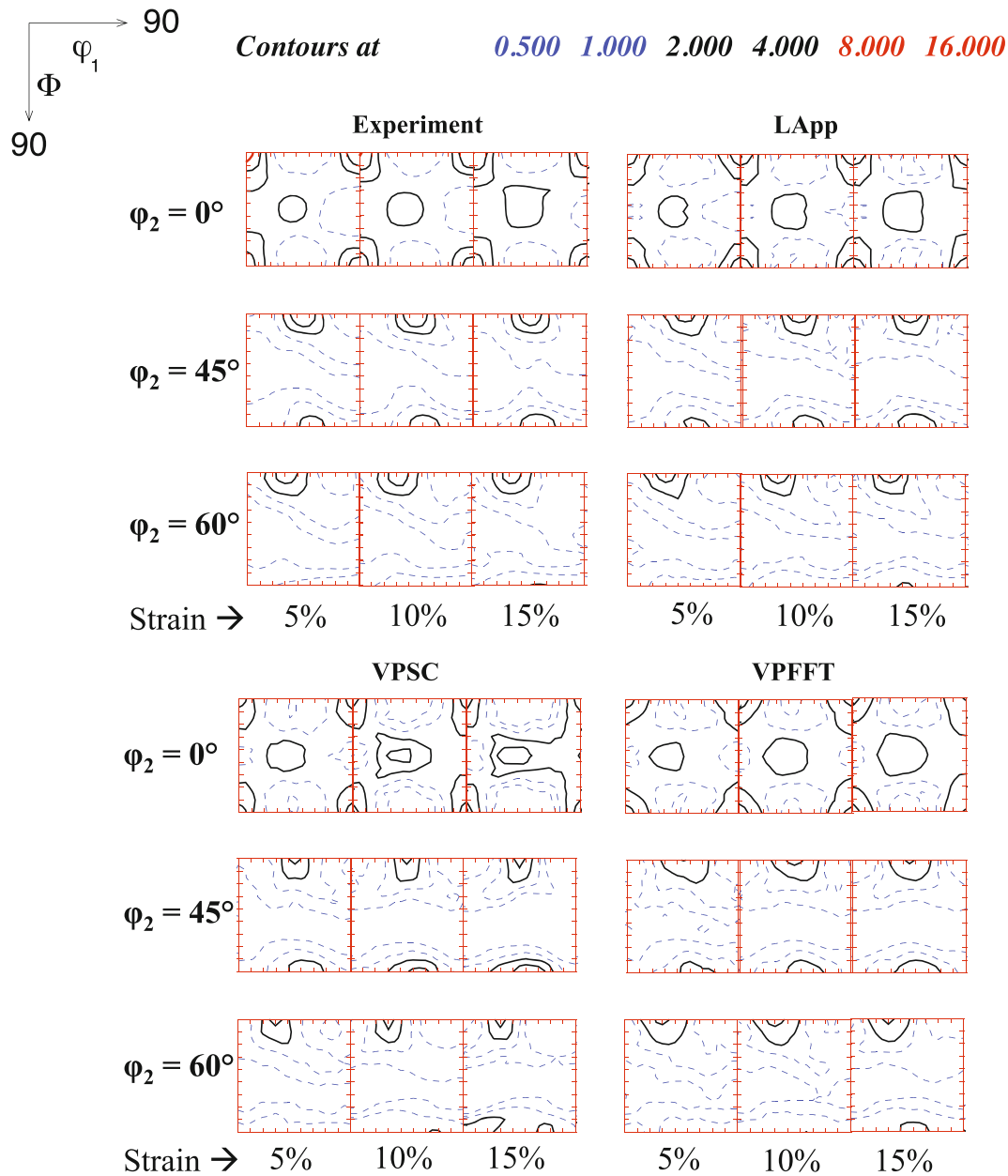


Fig. 13—Comparison of OD sections for TD-oriented plane strain tension. The strain levels are 5, 10, and 15 pct in TD.

The stress at the zero plastic strain level is influenced only by the texture and the initial CRSS  $\tau_0$ . In the simulation, it is independent of the initial hardening rate and the saturation CRSS since no strain hardening has yet occurred. Therefore, we can use the stresses at zero plastic strain to obtain the value of  $\tau_0$ . The error value is obtained by setting  $n = 0$  in Eq. [5], and thus, only the data points at zero plastic strain are included. Figure 2 shows the evolution of error values as  $\tau_0$  changes from 20 to 38 MPa with an increment of 1 MPa for the LApp simulation as an example. Each of the five stress-strain curves is associated with a minimum in error at a value of initial CRSS that does not necessarily coincide with the value corresponding to minimum in total error. However, averaging the five

individual errors does give a single minimum in the tested range (with no evidence of local minima), as shown by the solid line in Figure 2, and an optimal  $\tau_0 = 29$  MPa was identified, close to the individual minima for uniaxial and equibiaxial minima. The minimum error point lies at smaller strains, however, for the plane strain loading paths and corresponds to a shallower minimum in both cases.

The other two strain hardening parameters ( $\theta_0$  and  $\tau_1$  for the VPSC simulation in the example) are obtained in the same fashion. Error values are calculated by varying  $\theta_0$  and  $\tau_1$  simultaneously, and a best set of hardening parameters is found at the minimum, as shown in Figure 3. The optimal set of hardening parameters is found at  $\{\theta_0, \tau_1\} = \{310, 96\}$ .

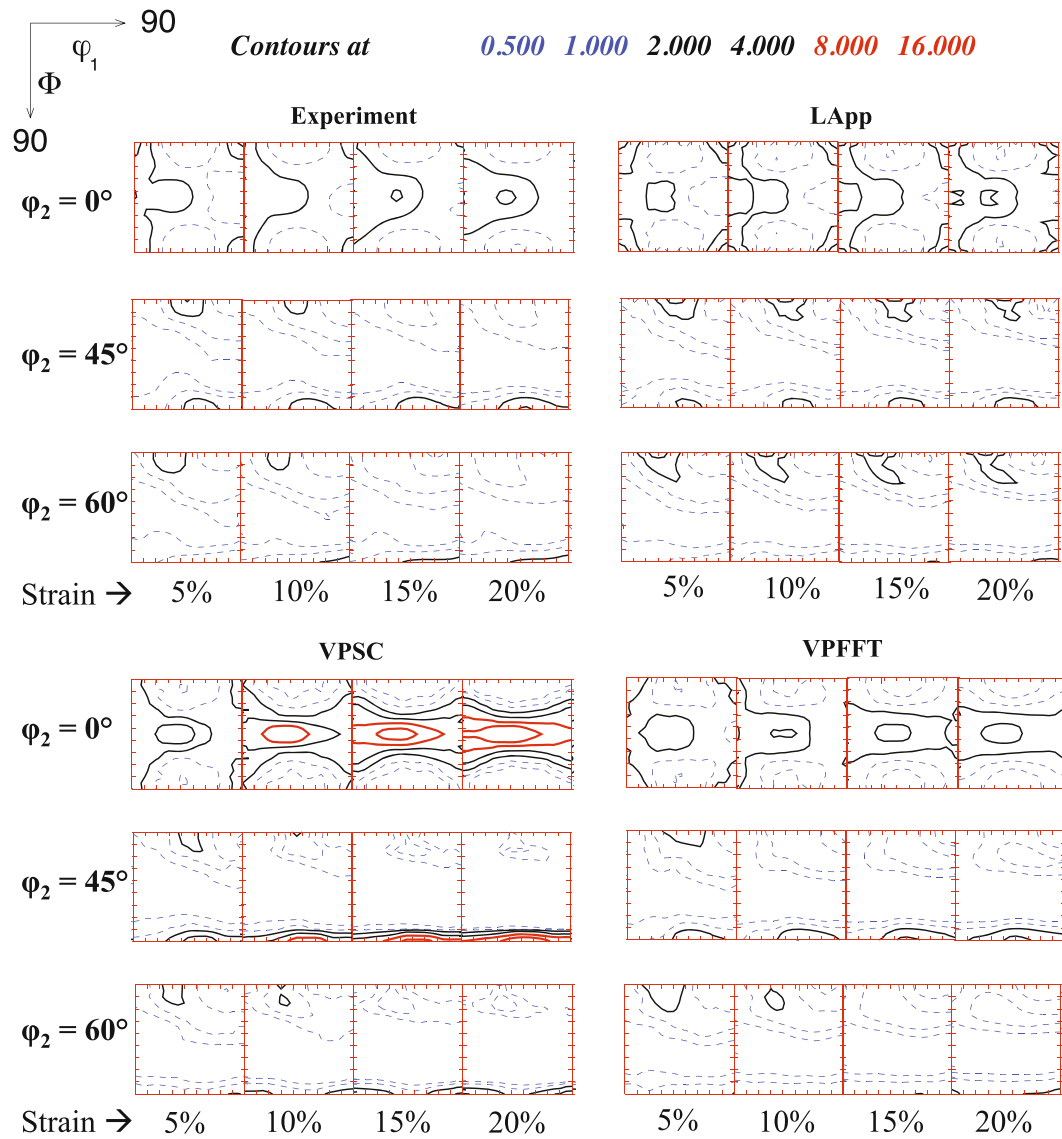


Fig. 14—Comparison of OD sections for equibiaxial stretch. The strain levels are 5, 10, 15, and 20 pct in RD (or TD, since strains in the two directions are the same).

Table IV. Bunge Euler Angles for Texture Components Along the  $\beta$ -Fiber (from Copper to Brass)

$\varphi_1$ (deg)	90	80	70	65	60	55	50	45	40	35
$\Phi$ (deg)	35	35.56	36.11	36.67	37.22	37.78	38.33	42.78	43.89	45
$\varphi_2$ (deg)	45	50	55	60	65	70	75	80	85	90

Parameters used in the three models are listed in Table III. Error values were also calculated in terms of absolute difference and CHI-square difference between the simulation and the experiment, but the resulting hardening parameter values were negligibly different from those fitted with the RMS error. It is also evident that the different models yielded similar parameter values as expected from the use of a similar law for all three codes.

## V. RESULTS AND DISCUSSION

### A. Stress-Strain Curve Predictions

Figures 4 through 8 depict the stress-strain curves for AA5754 in the aforementioned five deformation modes simulated by LApp, VPSC, and VPFET as well as those determined experimentally. The error bars shown for the experimental data are based on the measurement uncertainties determined for each data point individually, as

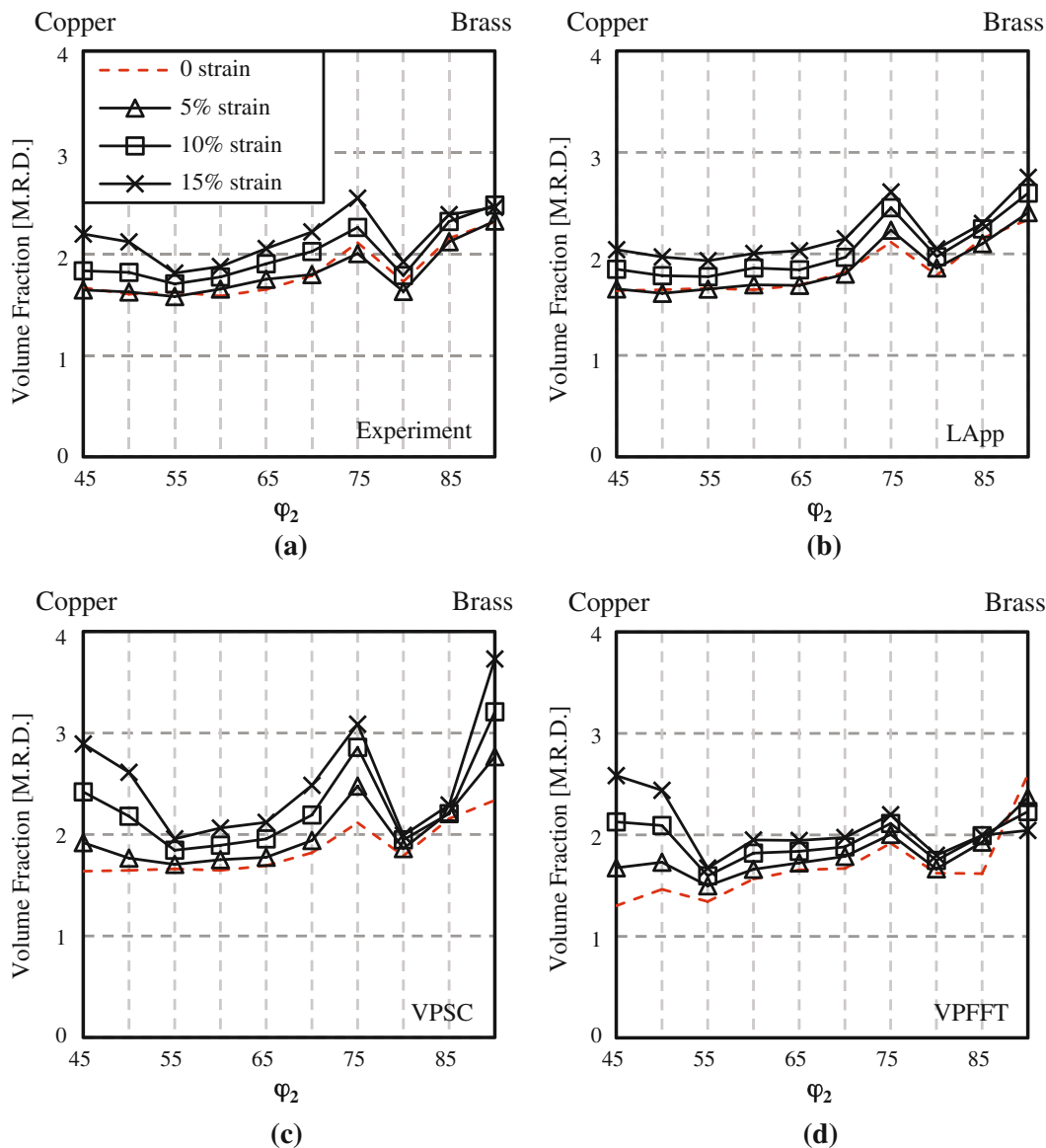


Fig. 15— $\beta$ -fiber volume fraction plots for the RD uniaxial tension from (a) the experiment, (b) the LApp simulation, (c) the VPSC simulation, and (d) the VPFFT simulation.

described in Iadicola *et al.*<sup>[15]</sup> The largest average experimental uncertainties seen are associated with the equibiaxial data ( $\pm 10$  MPa), and the smallest values are associated with the uniaxial data ( $\pm 6$  MPa). Looking at the simulation predictions, overall better fits are seen in VPSC and VPFFT than for the FC Taylor model. To summarize the differences quantitatively, the RMS errors associated with the quality of the fit to the experimental data are given in Figure 9 for each strain path and each model. The error value on the vertical axis is the RMS difference between the simulated stress-strain curves and the experimental data for each case. VPSC and VPFFT models give smaller error values (therefore better qualities of predictions), compared to the FC Taylor model.

With the same isotropic strain hardening behavior adopted in the three models, the better fitting from the

VPSC and VPFFT models suggests that incorporating the grain interaction improves the modeling of plastic deformation. However, for the two plane strain tension cases, for which stress was measured in two perpendicular directions, the VPSC and VPFFT models are often only able to closely match one of the two stresses, resulting in a root mean error larger than the average experimental uncertainty. The nontrivial deviation of calculated stresses from experimental data suggests the need to further analyze the strain hardening behavior or perhaps a more sophisticated hardening model. As far as the authors are aware, this represents the first time that plane strain experimental data of this type (that do not require specimen bending or the assumptions associated with a finite element model to determine the stress values) were used to develop constitutive relations.

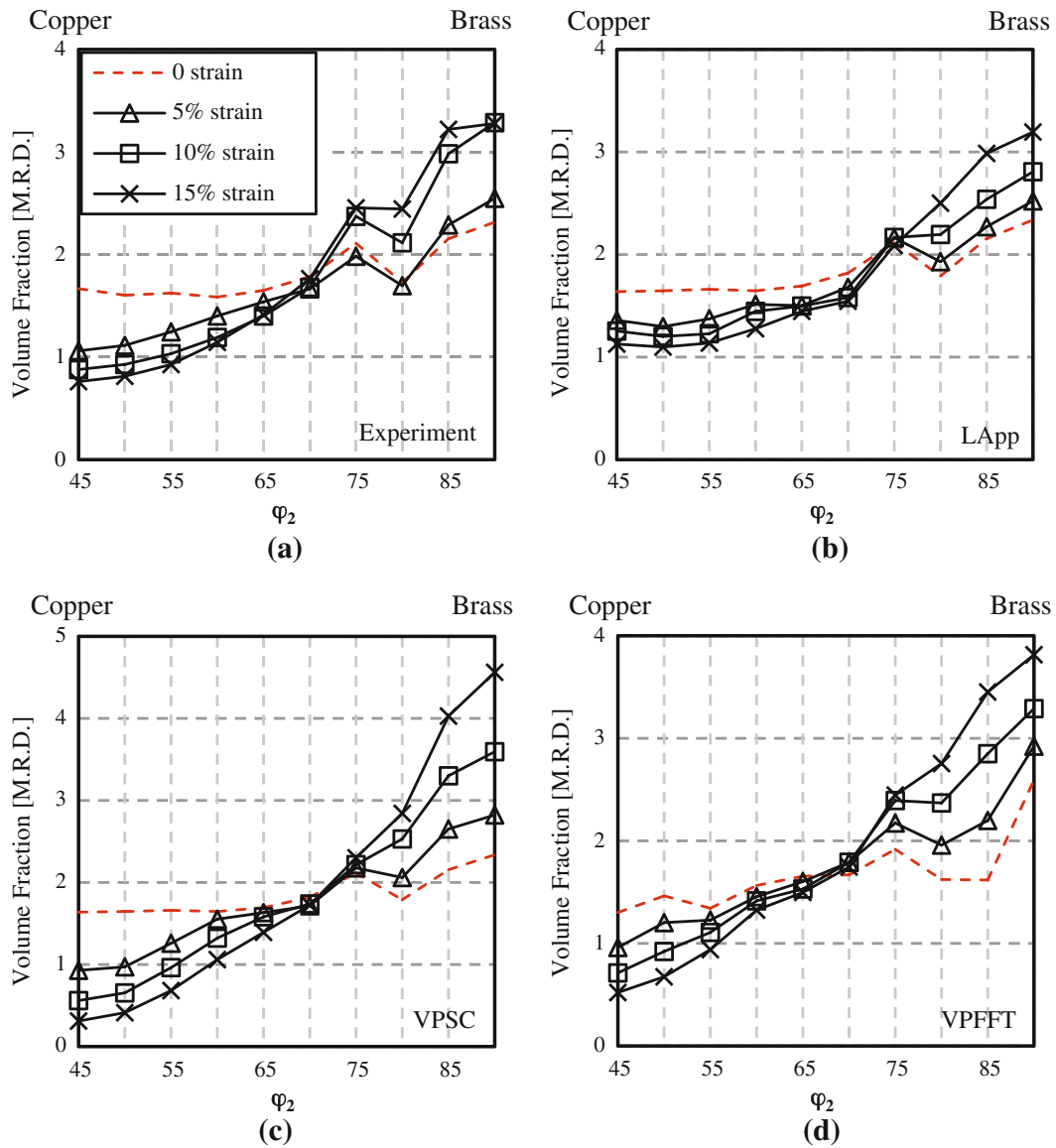


Fig. 16— $\beta$ -fiber volume fraction plots for the TD uniaxial tension from (a) the experiment, (b) the LApp simulation, (c) the VPSC simulation, and (d) the VPFFT simulation.

### B. Texture Evolution

Figures 10 through 14 demonstrate the development of OD as a function of deformation mode and strain level. 0, 45, and 60 deg  $\varphi_2$  sections in OD from experiments and simulations are compared at the same strain levels stated as follows: 5, 10, and 15 pct for uniaxial tension and plane strain, and 5, 10, 15, and 20 pct for equibiaxial stretch.

The following observations are made from the experimental ODs. For RD uniaxial tension, the strain is not large enough for the material to form complete  $\langle 100 \rangle$ -fiber and  $\langle 111 \rangle$ -fiber. The material starts with a  $\beta$ -fiber texture, and components along the  $\beta$ -fiber parallel to  $\langle 100 \rangle$  or  $\langle 111 \rangle$  directions intensify. For TD uniaxial tension, grains tend to rotate to the Cube and Brass orientations. The  $\beta$ -fiber further develops in the RD plane strain. Grains move toward the Brass orientation

in TD-oriented plane strain.  $\langle 110 \rangle$  crystal axes gradually aligned with the sample ND in the equibiaxial stretch, forming a  $\langle 110 \rangle$ -fiber texture. Qualitatively, the three plasticity models predict the same patterns, except for the equibiaxial stretch, where the FC Taylor model fails to predict the removal of cube orientations.

The simulated evolution of texture intensities varies markedly among the models. To quantify the texture evolution, volume fractions along the beta fiber are calculated for uniaxial tension and plane strain cases. Table IV lists the Bunge Euler angles for the ten points chosen along the fiber. Since the development of a  $\langle 110 \rangle$ -fiber is most prominent in the equibiaxial stretch test, orientations along the  $\langle 110 \rangle$ -fiber ( $\varphi_1 = 0$  to 35 deg,  $\Phi = 45$  deg, and  $\varphi_2 = 0$  deg) are selected instead for this strain state. The fiber volume fraction plots are shown in Figures 15 through 19. We can see that, in

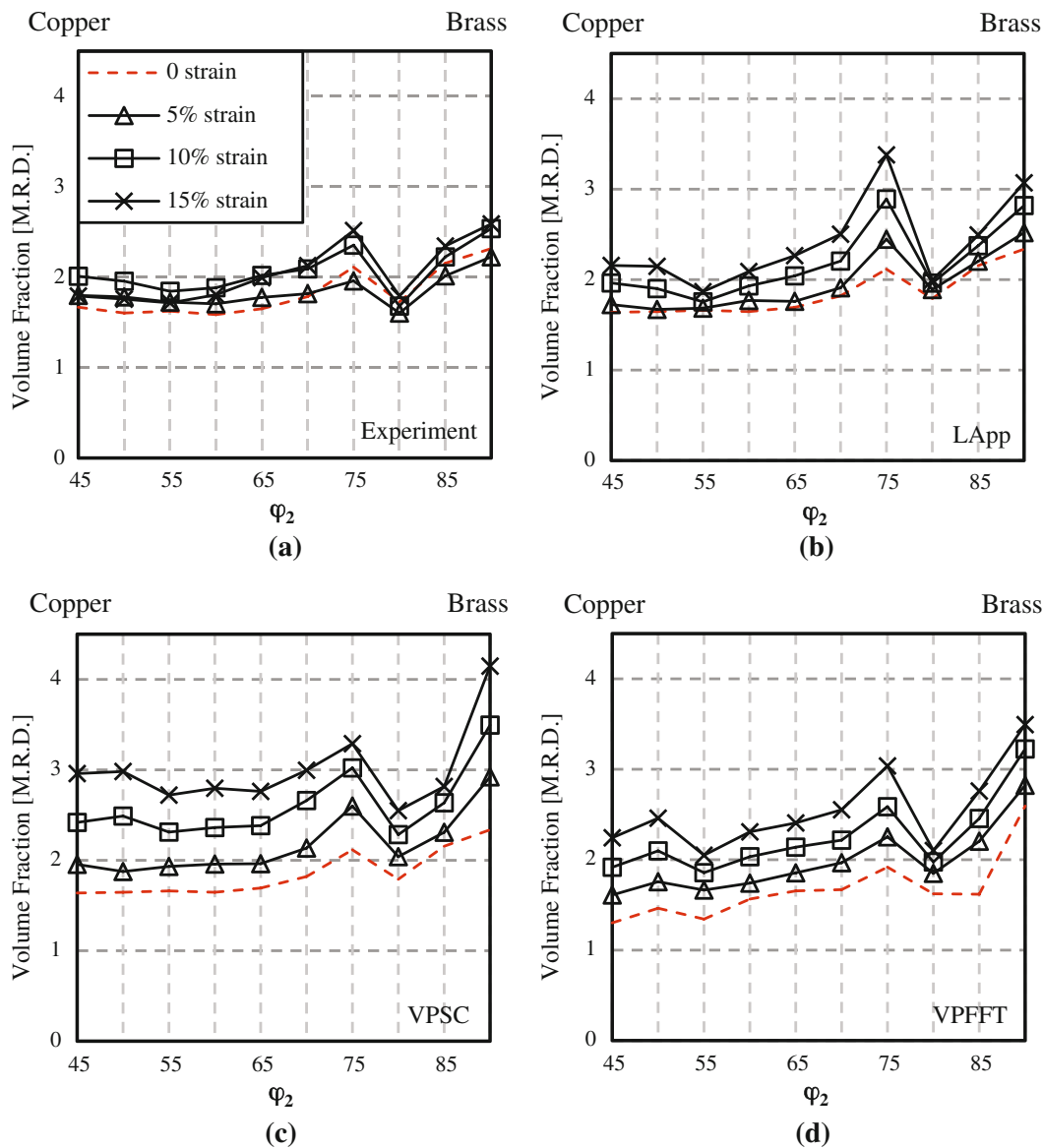


Fig. 17— $\beta$ -fiber volume fraction plots for the RD-oriented plane strain from (a) the experiment, (b) the LApp simulation, (c) the VPSC simulation, and (d) the VPFFT simulation.

general, the VPSC simulation results in volume fractions much higher than experiment (note the change in scale for the VPSC results), while the LApp simulation is quite reliable for uniaxial and plane strain cases, and the VPFFT model appears to capture more of the overall development in most cases.

The VPSC model we used in the study is essentially a one-site model. The grain interaction is dealt with in an average sense and no special treatment is given to the local environment. Therefore, grains with the same orientation, but different neighbors, will deform in a same way. It is similar to the FC Taylor model for texture simulation in the sense that grains with the same initial orientations will rotate in the same fashion, leading to orientation concentrations and thus higher predicted texture intensities than those seen in the

experiment.<sup>[20]</sup> A major difference between the FC Taylor model and the tangent one-site VPSC model is the assumption on the grain interaction. The FC Taylor model assumes a completely stiff body, while the tangent VPSC model assumes a relatively compliant grain to matrix interaction. Therefore, it appears that the faster texture evolution seen in the VPSC simulation is due to its overestimate of the matrix compliance. On the other hand, it is worth mentioning that the FC Taylor model fails to predict the removal of cube orientations in equibiaxial tension, while the VPSC model captures the correct texture evolution. This finding indicates that the actual interaction behavior might be between the complete stiffness assumed in the FC Taylor model and the tangent behavior. Intermediate interaction schemes include stiffer inclusion to matrix formulations such as

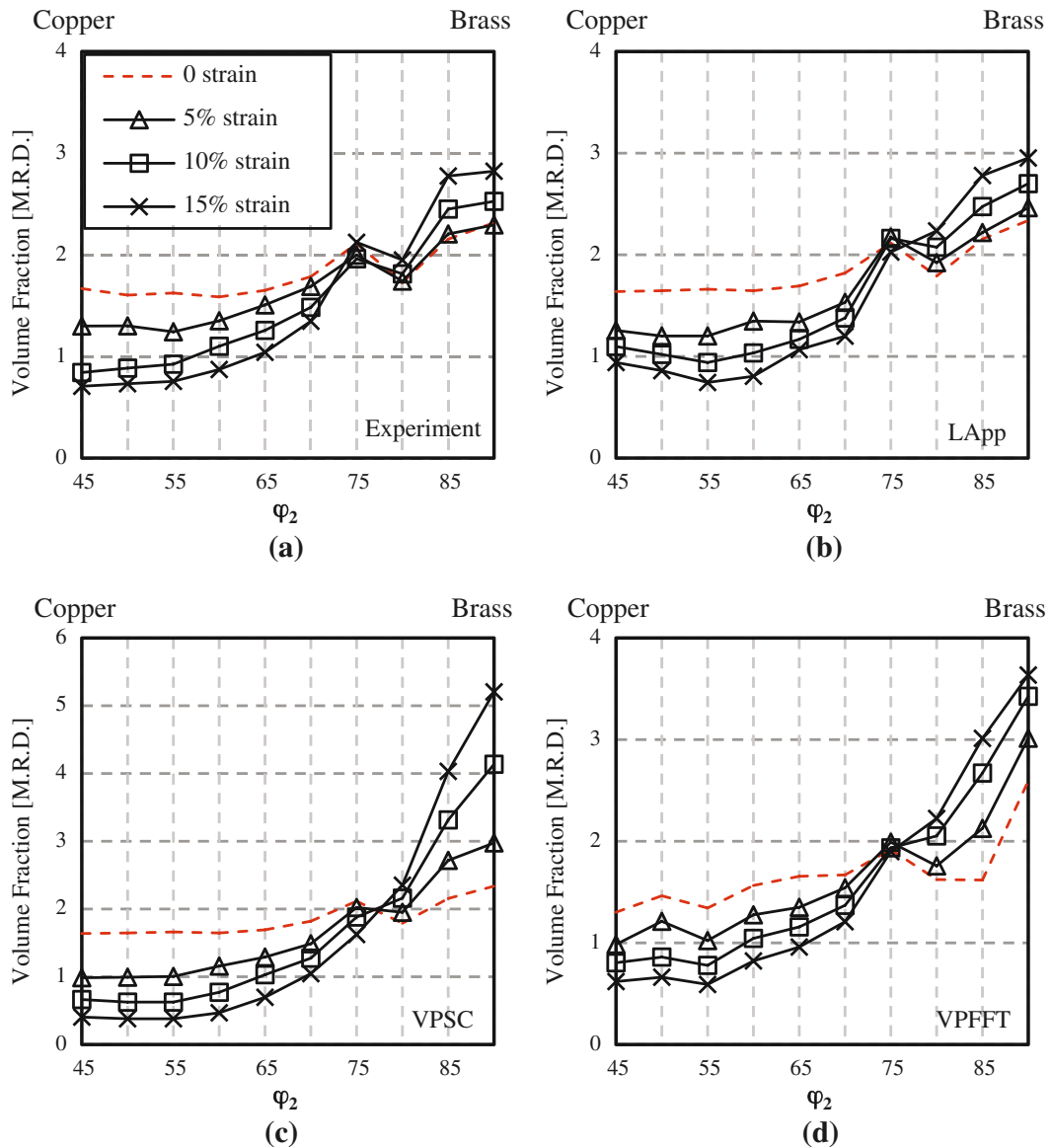


Fig. 18— $\beta$ -fiber volume fraction plots for the TD-oriented plane strain from (a) the experiment, (b) the LApp simulation, (c) the VPSC simulation, and (d) the VPFFT simulation. Note the scale change in (c) the VPSC plot.

the secant<sup>[21]</sup> and affine<sup>[22]</sup> approaches. The prediction of a more pronounced texture by the tangent VPSC model is also reported by M'Guil *et al.*<sup>[23]</sup> for deformation texture in tension and compression and also by Li *et al.*<sup>[20]</sup> for the texture evolution in copper during equal channel angular extrusion. It has been further shown that to weaken the texture evolution prediction in the VPSC model, grain-grain interaction needs to be accounted for in more detail, such as incorporating a grain co-rotation scheme<sup>[24]</sup> for orientation correlations or implementing a rule for grain subdivisions.<sup>[25]</sup>

The improvement by the N-site VPFFT model is largely due to the fact that voxels in a grain are allowed to deform differently such that internal orientation gradients can develop within grains. This effectively increases the spread in grain orientations and retards the texture development.

### C. Lankford Coefficient Comparison

As a further check of the quality of the simulations, a comparison is made between predicted and measured values of the Lankford coefficient. Otherwise known as the  $R$  value, it measures the plastic anisotropy in the material. It is defined as the ratio of the width plastic strain to the through-thickness plastic strain in a uniaxial tensile test. Using the material parameters we obtained from the stress-strain curve fitting, we were able to compute  $R$  values for the tested material, as shown in Figure 20. The  $R$  values were calculated with both the LApp code and the tangent VPSC code, at an angular interval of 15 deg (the use of stress boundary conditions on the overall polycrystal in the VPFFT code was not implemented, which is what is required for the  $R$ -value calculation). When compared to the experimental values

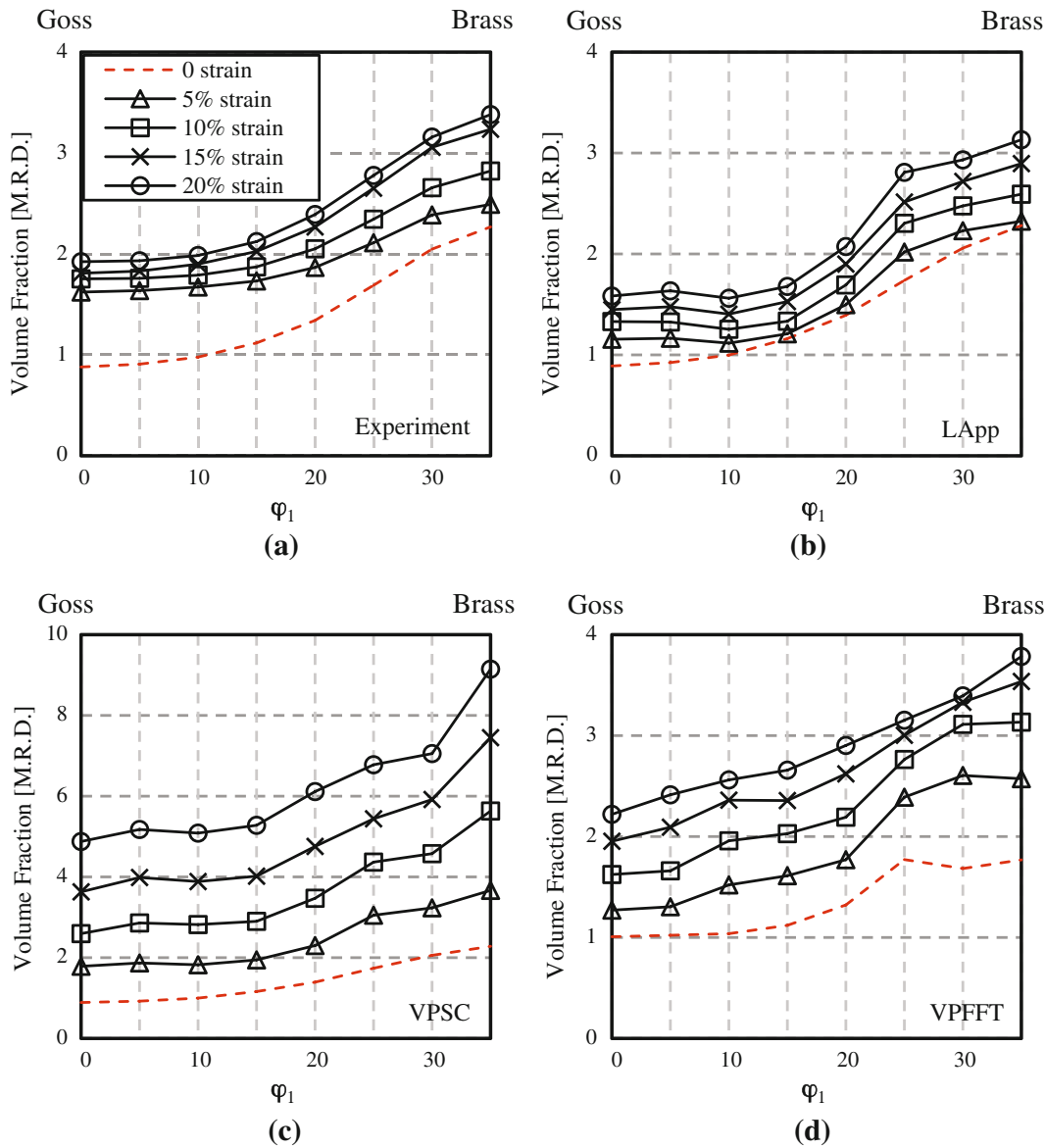


Fig. 19— $\langle 110 \rangle$ -fiber ( $\phi_1 = 0$  to  $35$  deg,  $\Phi = 45$  deg, and  $\phi_2 = 0$  deg) volume fraction plots for equibiaxial stretch from (a) the experiment, (b) the LApp simulation, (c) the VPSC simulation, and (d) the VPFFT simulation. Note the scale change in (c) the VPSC plot.

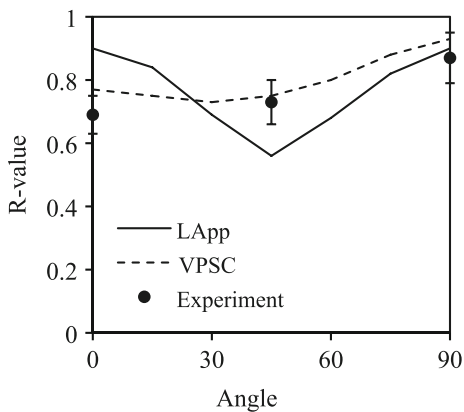


Fig. 20—Calculated  $R$  values vs the angle between the rolling direction and the stressing direction, with experimental values and error bars for comparison.

in Figure 20, the calculated values show relatively good agreement, particularly considering that no parameter adjustments were made in the model to optimize the fits to compare to the Lankford coefficient. Bate and An<sup>[26]</sup> compared the measured  $R$  value in AA5005 with the Taylor model predictions and showed similar deviations.

## VI. CONCLUSIONS

Plastic deformation under various strain paths for AA5754 aluminum alloy was simulated with the FC Taylor model, a tangent VPSC model, and the N-site VPFFT model. The single slip system hardening parameters were fitted by comparison with the experimental stress-strain curves. It was shown that allowing stress and strain variations in grains improved multiaxial

stress-strain predictions. Texture development was also compared with experiments both qualitatively and quantitatively. Overall, the N-site VPFFT model had the best texture prediction. The results indicate that taking grain interaction into consideration refines the polycrystal plasticity modeling. However, the failure to predict the mechanical response equally well for all the different multiaxial loading paths points out the need to find more effective ways to describe accurately the strain hardening.

#### ACKNOWLEDGMENTS

This work was supported at Carnegie Mellon University by the National Institute of Standards & Technology under Award No. 70NANB8H8038. Use of facilities provided by the Higher Education Program, Intel Corporation, and by the MRSEC, CMU, under NSF Grant No. DMR-0520425 is also gratefully acknowledged. Use of the VPFFT code from Ricardo Lebensohn, Los Alamos National Laboratory, is gratefully acknowledged.

#### REFERENCES

1. W.S. Miller, L. Zhuang, and J. Bottema: *Mater. Sci. Eng. A*, 2000, vol. 280, pp. 37–49.
2. G.I. Taylor: *J. Inst. Met.*, 1938, vol. 62, pp. 307–24.
3. R.J. Asaro and A. Needleman: *Acta Metall.*, 1985, vol. 33 (6), pp. 923–53.
4. Los Alamos Polycrystal Plasticity Code, Los Alamos National Laboratory LA-CC-88-6, Los Alamos, NM, 1988.
5. U.F. Kocks, M.G. Stout, and A.D. Rollett: *Proc. 8th Int. Conf. on the Strength of Metals and Alloys*, Pergamon Press, Tampere, Finland, 1988, pp. 23–34.
6. C.A. Bronkhorst, S.R. Kalidindi, and L. Anand: *Phys. Sci. Eng.*, 1992, vol. 341 (1662), pp. 443–77.
7. A. Molinari, G.R. Canova, and S. Ahzi: *Acta Metall.*, 1987, vol. 35, pp. 2983–94.
8. R.A. Lebensohn and C.N. Tomé: *Acta Metall.*, 1993, vol. 41 (9), pp. 2611–24.
9. S.H. Choi, J.C. Brem, F. Barlat, and K.H. Oh: *Acta Mater.*, 2000, vol. 48, pp. 1853–63.
10. H. Moulinec and P. Suquet: *Comput. Meth. Appl. Mech. Eng.*, 1998, vol. 157, pp. 68–94.
11. R.A. Lebensohn: *Acta Mater.*, 2001, vol. 21, pp. 2723–37.
12. L. Delannay, S.R. Kalidindi, and P. Van Houtte: *Mater. Sci. Eng. A*, 2002, vol. 336, pp. 233–44.
13. *ASM Handbook: Properties and Selection: Nonferrous Alloys and Special-Purpose Materials*, ASM INTERNATIONAL, Materials Park, OH, 1990, vol. 2, pp. 37–52.
14. T. Foecke, M.A. Iadicola, A. Lin, and S.W. Banovic: *Metall. Mater. Trans. A*, 2007, vol. 38A, pp. 306–13.
15. M.A. Iadicola, T. Foecke, and S.W. Banovic: *Int. J. Plast.*, 2008, vol. 24 (11), pp. 2084–2101.
16. S.W. Banovic, M.A. Iadicola, and T. Foecke: *Metall. Mater. Trans. A*, 2008, vol. 39A, pp. 2246–58.
17. J.S. Kallend, U.F. Kocks, A.D. Rollett, and H.R. Wenk: *Mater. Sci. Eng. A*, 1991, vol. 132, pp. 1–11.
18. C.N. Tomé: *Model. Simul. Sci. Eng.*, 1999, vol. 7, pp. 723–38.
19. A. Brahme, M.H. Alvi, D. Saylor, J. Fridy, and A.D. Rollett: *Scripta Mater.*, 2006, vol. 55, pp. 75–80.
20. S. Li, I.J. Beyerlein, D.J. Alexander, and S.C. Vogel: *Acta Mater.*, 2005, vol. 53, pp. 2111–25.
21. R.A. Lebensohn and C.N. Tomé: *Mater. Sci. Eng. A*, 1994, vol. 175 (1–2), pp. 71–82.
22. R. Masson, M. Bornert, P. Suquet, and A. Zaoui: *J. Mech. Phys. Solids*, 2000, vol. 48, pp. 1203–27.
23. S. M'Guil, S. Ahzi, H. Youssef, J. Gracio, and M.A. Khaleel: *Mater. Sci. Forum*, 2007, vol. 553, pp. 81–86.
24. C.N. Tomé, R.A. Lebensohn, and C.T. Necker: *Metall. Mater. Trans. A*, 2002, vol. 33A, pp. 2635–48.
25. I.J. Beyerlein, R.A. Lebensohn, and C.N. Tomé: *Mater. Sci. Eng.*, 2003, vol. 345, pp. 122–38.
26. P.S. Bate and Y.G. An: *Scripta Mater.*, 2004, vol. 51, pp. 973–77.